catalysts

MDPI

Article

Effects of ZSM-5 Morphology and Fe Promoter for Dimethyl Ether Conversion to Gasoline-Range Hydrocarbons

Mansoor Ali, Jong Jin Kim, Faisal Zafar, Dongming Shen, Xu Wang and Jong Wook Bae *

School of Chemical Engineering, Sungkyunkwan University (SKKU), 2066 Seobu-ro, Jangan-gu, Suwon 16419, Republic of Korea

* Correspondence: finejw@skku.edu; Tel.: +82-31-290-7347; Fax: +82-31-290-7272

Abstract: The synthesis of gasoline-range hydrocarbons by gas-phase dimethyl ether (DME) conversion was investigated on various ZSM-5 zeolites with different morphologies and Fe contents. The different morphologies of ZSM-5 significantly altered the distributions of the acidic sites, which showed different selectivities to gasoline-range hydrocarbons. Nanostructured ZSM-5 (N-ZSM-5) revealed the highest C_{5+} selectivity of 41.7% with an aromatics selectivity of 23.6% at ~100% DME conversion. The superior catalytic activity of N-ZSM-5 was attributed to the largest strong Brønsted acidic sites and smaller crystallite sizes, which were beneficial for the faster removal rate of heavy hydrocarbons due to its shorter diffusion pathlength compared to conventional ZSM-5 (C-ZSM-5). In addition, 10 wt% Fe-impregnated N-ZSM-5 revealed an enhanced C_{5+} selectivity of 60.6% with a smaller C_1–C_4 selectivity of 21.9%, which were attributed to the adjusted acidic sites by suppressing the cracking reactions of the surface intermediates, which are responsible for the selective formation of smaller light hydrocarbons. However, the excess amount of Fe on N-ZSM-5 showed a lower DME conversion of 83.5% with a lower C_{5+} selectivity of 38.5% due to the blockages of the active acidic sites. Nanostructured N-ZSM-5 possessing a larger amount of strong Brønsted acid sites with 10 wt% Fe modification clearly showed a higher formation rate of gasoline-range hydrocarbons due to an enhanced secondary oligomerization of surface intermediates to form heavier aromatic hydrocarbons.

Keywords: conversion of dimethyl ether (DME); gasoline-range hydrocarbons; morphology of ZSM-5; Fe-modified ZSM-5; surface acidity

Citation: Ali, M.; Kim, J.J.; Zafar, F.; Shen, D.; Wang, X.; Bae, J.W. Effects of ZSM-5 Morphology and Fe Promoter for Dimethyl Ether Conversion to Gasoline-Range Hydrocarbons. *Catalysts* **2023**, *13*, 910. https://doi.org/10.3390/catal13050910

Academic Editors: Ning Rui and Lili Lin

Received: 14 April 2023
Revised: 14 May 2023
Accepted: 16 May 2023
Published: 21 May 2023

1. Introduction

With the fast-paced growth of the transportation sector and the consequent increase in CO_2 emissions from both transportation and industry, it has become important to explore alternative resources in light of the higher demand for liquid fuels and the ongoing depletion of conventional fossil fuels [1]. There has been an increasing focus on exploring environmentally benign methods to convert raw feedstock such as biomass, natural gas, or coal into clean fuels and petrochemicals. Methanol, a feedstock for the methanol-to-hydrocarbon (MTH) reaction via the dimethyl ether (DME) route, has been commercially produced by syngas conversion. Generally, an indirect two-step process of DME synthesis via methanol dehydration seems to be less efficient due to its thermodynamic limitations, and the direct one-step conversion of syngas to DME (STD) has emerged as a more promising alternative way due to its small investment cost, low power consumption, and improved one-pass CO conversion [2–8]. Therefore, many studies have focused on the conversion of DME to clean transportation fuels such as gasoline-range hydrocarbons on various solid acid zeolites via a one-step STD reaction [9,10]. In addition, the recent techno-economic analysis of the DME-to-gasoline (DTG) process has suggested its higher economic feasibility by utilizing biomass or coal-derived syngas [11,12]. It has been reported that zeolites having unique shape selectivity and surface acidity play important roles in DME conversion to gasoline-range hydrocarbons by multiple reaction steps such as surface methyl formation,

olefin methylation, olefin cracking, hydrogen transfer, cyclization, aromatics methylation, aromatics dealkylation, and so on [13,14]. In particular, ZSM-5 with MFI topology was found to be crucial for the selective production of gasoline-range hydrocarbons due to its unique channel structures with medium pore size openings, which are important for the selective penetrations of intermediates in the pores, resulting in the shape-selective formation of gasoline-range hydrocarbons [15]. The ZSM-5 frameworks were composed of two kinds of intersecting 10-membered ring channels, straight channels (5.6×5.3 Å^2) along the crystallographic *b*-axis interconnected with sinusoidal channels (5.5×5.1 Å^2) along the *a*-axis [16]. Among the various zeolites, ZSM-5 with unique structure has been a subject of interest because of its unique catalytic properties for various catalytic reactions such as methanol/DME to gasoline (MTG/DTG), methanol/DME to aromatics (MTA/DTA), methanol/DME to olefins (MTO/DTO) [17–23], xylene isomerization [24], aromatic alkylation [25], distillate dewaxing [26], and upgrading of Fischer–Tropsch synthesis products [27]. Besides the zeolite topology, the morphology of zeolites also plays a crucial role in adjusting the product distributions by changing the diffusion rates of reactants and products on the acidic surfaces [28], where the diffusion proficiency of intermediates largely changes the catalytic activity and product distributions [29–31]. For example, nanocrystal ZSM-5 can improve the catalyst lifetime and liquid hydrocarbon yield for the MTG reaction more than micro-sized ZSM-5 due to lower molecular diffusion hindrance [32], and hierarchically structured ZSM-5 zeolite also changes the aromatic distributions of the syngas-to-aromatics (STA) reaction by altering pore structures and surface acidity [33]. Aromatic selectivity can also be increased by adjusting the length of crystallites of sheet-like ZSM-5 for the STA reaction [34].

Since the DTG/MTG reaction on ZSM-5 generally produces aromatic-rich hydrocarbons, the desired aliphatic gasoline-range hydrocarbons from oxygenates can be further formed by its successive secondary hydrogenation and isomerization reaction, which can be possibly realized by metal modifications to enhance DTG reaction performances [35,36]. The incorporation of metallic heteroatoms such as Zn, Mn, Co, and Cr significantly enhances the hydrogen transfer and aromatization activity of the modified zeolites, which further increases the gasoline-range hydrocarbon selectivity for the DTG reaction [37–40]. Among these various metal promoters, Fe-modified ZSM-5 has been extensively reported with enhanced activity for STA [41], MTG [42], and methane dehydroaromatization (MDA) [43], where the incorporation of the Fe species in nanocrystalline H[Fe,Al]ZSM-5 significantly improved catalytic performances for the DTG reaction by selectively reducing aromatic selectivity [44–47]. In the present study, the effects of the different morphologies of ZSM-5 zeolites, such as rectangular (N-ZSM-5), hexagonal (H-ZSM-5), sheet-like (S-ZSM-5), and sphere-like (C-ZSM-5) structures, with the incorporation of Fe metal oxides on the selected N-ZSM-5 zeolite were studied to verify the roles of ZSM-5 morphology on catalytic activity and gasoline-range hydrocarbon selectivity during the DTG reaction.

2. Results and Discussion

2.1. Structural and Surface Acidic Property of ZSM-5 Zeolites

The effects of the different ZSM-5 morphologies and additional Fe modification to change the textural and surface acidic properties were investigated with N_2-sorption, PXRD, SEM, and TEM analysis. The PXRD patterns on all fresh ZSM-5, as displayed in Figure 1A, reveal the characteristic diffraction peaks of MFI zeolitic structures [48] without any distinctive impurity peaks. As summarized in Table 1, the relative crystallinity calculated from the most intense diffraction peaks at $2\theta = 7–9^\circ$ was found to be smaller on ZSM-5 in the range of 29–71% based on 100% of most crystalline S-ZSM-5, which was attributed to their different morphologies and smaller average nanoscale grain sizes in the range of 83–300 nm compared to that of 1.67 μm on S-ZSM-5. The observed lower crystallinity of 68% and smaller crystallite size of 32 nm on N-ZSM-5 compared to those on S-ZSM-5 45 nm in size were also attributed to its lower Si/Al ratio of 72 (Si/Al ratio of 94 on S-ZSM-5), as confirmed by XRF analysis. In addition, the slight shifts in diffraction peak

positions from those on C-ZSM-5, as shown in Supplementary Figure S3, can be attributed to the possible substitution of smaller Al cations in the crystalline structures of N-ZSM-5 and S-ZSM-5, which resulted in an increased *d*–spacing parameter between the lattice planes with larger amounts of acidic sites. As displayed in Figure 1B, the PXRD patterns on fresh Fe/N-ZSM-5 also showed the characteristic diffraction peaks of the ZSM-5 and Fe_2O_3 phases, which also suggests that the MFI structures of N-ZSM-5 were stably preserved even after the incorporation of Fe species. The crystallite sizes of ZSM-5, as summarized in Table 2, were increased with an increase in Fe content from 32 nm on pristine N-ZSM-5 to 46 nm on Fe(15)/N-ZSM-5 with an inverse trend of a monotonous decrease in crystallinity from 68% to 21% due to the possible structural collapses of N-ZSM-5 with the incorporation of iron oxides, where the diffraction peaks at 2θ = 33.1, 35.6, 40.8, 49.5, and 54.1° are separately assigned to the (104), (110), (113), (024), and (116) facets of Fe_2O_3 hematite (JCPDS No. 033-0664) [49]. In addition, the decreased intensity of these diffraction peaks with an increase in Fe content was attributed to the increased crystallite size of ZSM-5 on the Fe/N-ZSM-5 surfaces (from 32 nm on N-ZSM-5 to 38–46 nm on Fe/N-ZSM-5) due to an excess amount of Fe_2O_3 phases and its structural disintegrations, as shown in Figure 1B.

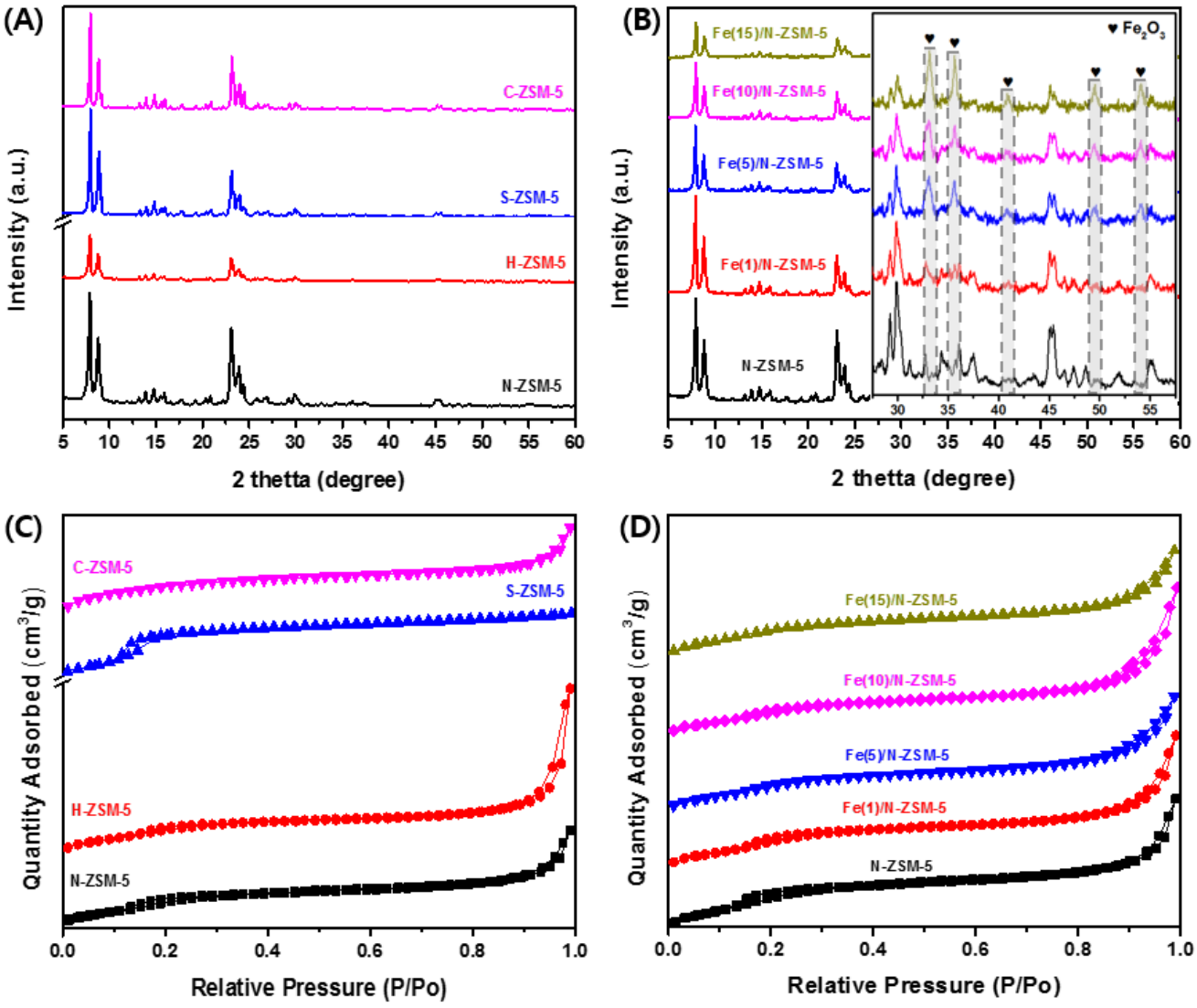

Figure 1. Characteristics of four different ZSM-5 and Fe/N-ZSM-5 zeolites: (**A**) PXRD patterns of fresh ZSM-5, (**B**) PXRD patterns of fresh Fe/N-ZSM-5, (**C**) N_2 adsorption–desorption isotherms of fresh ZSM-5, and (**D**) N_2 adsorption–desorption isotherms of Fe/N-ZSM-5.

Table 1. Bulk and surface properties of ZSM-5 zeolites with their different morphologies and catalytic performance of DTG reaction.

Catalyst	XRF [a]	XRD [b]		N_2-Sorption [c]			NH_3-TPD [d]	Py-IR [e]		X_{DME} (mol%)	Selectivity [f]
	Si/Al Ratio	S_{cryst} (nm)	R_{cryst} (%)	S_g/S_{ext} (m^2/g)	V_P/V_{meso} (cm^3/g)	P_D (nm)	W/M/S (Total) (mmol/g)	B/L (μmol/g)	B/L Ratio		C_1–C_4/C_{5+}/Aro
N-ZSM-5	72	32	68	366/196	0.29/0.20	4.1	0.32/0.0/0.16 (0.48)	159.9/4.5	32.2	100	34.7/41.7/23.6
H-ZSM-5	74	34	29	376/177	0.40/0.29	7.2	0.23/0.06/0.06 (0.35)	84.3/5.4	15.5	100	37.1/41.0/21.9
S-ZSM-5	94	45	100	347/232	0.10/0.04	3.9	0.19/0.0/0.12 (0.31)	48.4/4.3	11.4	100	43.4/38.1/18.5
C-ZSM-5	84	69	71	360/94	0.24/0/10	4.6	0.32/0.0/0.13 (0.45)	84.8/4.1	20.7	100	39.5/40.5/20.0

[a] Si/Al molar ratio on fresh ZSM-5 with different morphologies was determined by XRF analysis, and H-form ZSM-5 zeolites were denoted as follows: N-ZSM5 for nanostructured H-form ZSM-5, H-ZSM5 for hierarchically structured ZSM5, S-ZSM5 for sheet-structured ZSM-5, and C-ZSM5 for conventional ZSM-5. [b] Crystallite size ($S_{crystal}$, nm) of ZSM-5 grains on different ZSM-5 zeolites was calculated from most intense characteristic diffraction peaks, and relative crystallinity (R_{cryst}, %) was calculated by using ratios of most intense diffraction peaks at 2θ = 7–9° based on crystallinity of 100% on S-ZSM-5. [c] S_g and S_{ext} (m^2/g) were measured by N_2-sorption analysis with help of BET method and t-plot method, where S_{ext} represents external surface area by subtracting micropore area from t-plot method. V_P and V_{meso} (cm^3/g) represent total pore and mesopore volume determined from adsorbed amount at P/P_0 = 0.995 by t-plot method. P_D (nm) represents average pore diameter. [d] Quantity of weak (W), medium (M), and strong (S) acid sites with total amount was determined by NH_3-TPD analysis by quantifying desorbed amounts of NH_3 probe molecules at 120–250 and 250–550 °C, respectively. [e] Quantity of Brønsted acid sites (B) and Lewis acid sites (L), as well as B/L ratios, was measured by pyridine FT-IR (Py-IR) analysis; concentration was estimated by using Py-IR peak area at 1540 and 1490 cm^{-1} at desorption temperature of 350 °C, respectively. [f] DTG reaction activity (DME to gasoline-range hydrocarbons with almost 100% DME conversion (X_{DME}) with hydrocarbon distributions including aromatics (Aro)) was measured at T = 290 °C, P = 0.1 MPa, and space velocity (SV) = 4400 L/(kg_{cat}·h) with feed reactant of DME/N_2 = 5/95 (mol%).

Table 2. Bulk and surface properties and catalytic activity for DME conversion to gasoline-range hydrocarbons on Fe/N-ZSM-5.

Catalyst	XRD [a]			N_2-Sorption [b]			NH_3-TPD [c]	Catalytic Activity (mol%) [d]	
	S_{cryst} (nm)		R_{cryst} (%)	S_g/S_{ext} (m^2/g)	V_P/V_{meso} (cm^3/g)	P_D (nm)	W/S (Total) (mmol/g)	X_{DME} (mol%)	Product Distribution (mol%) (C_1–C_4/C_5/C_{6+} (Aromatics))
	N-ZSM-5	Fe_2O_3							
N-ZSM-5	32	-	68	366/196	0.29/0.20	4.1	0.32/0.16 (0.48)	100.0	34.7/12.8/52.5 (23.6)
Fe(1)/N-ZSM-5	38	-	65	341/173	0.29/0.20	4.9	0.31/0.15 (0.46)	100.0	38.2/11.5/50.3 (20.3)
Fe(5)/N-ZSM-5	42	8.7	55	316/150	0.25/0.16	4.7	0.23/0.13 (0.36)	91.7	38.3/9.3/52.4 (18.3)
Fe(10)/N-ZSM-5	46	11.1	36	310/145	0.24/0/16	4.8	0.21/0.10 (0.31)	100.0	21.9/8.5/69.6 (17.6)
Fe(15)/N-ZSM-5	46	13.6	21	294/141	0.24/0.16	6.0	0.18/0.10 (0.27)	83.5	44.5/7.8/47.7 (17.0)

[a] Crystallite size ($S_{crystal}$, nm) of ZSM-5 grains on different ZSM-5 zeolites was calculated from most intense characteristic diffraction peaks, and crystallite size of Fe_2O_3 was estimated from most intense peak at 2θ = 35.6°. Relative crystallinity (R_{cryst}, %) was calculated by using ratios of most intense diffraction peaks at 2θ = 7–9° based on crystallinity of 100% on S-ZSM-5. [b] S_g and S_{ext} (m^2/g) were measured by N_2-sorption analysis with help of BET method and t-plot method, where S_{ext} represents external surface area by subtracting micropore area from t-plot method. V_P and V_{meso} (cm^3/g) represent total pore and mesopore volume determined from adsorbed amount at P/P_0 = 0.995 by t-plot method, and P_D (nm) represents average pore diameter. [c] Quantity of weak (W) and strong (S) acid sites with total amount was determined by NH_3-TPD analysis by quantifying desorbed amounts of NH_3 probe molecules at 120–250 and 250–550 °C, respectively. [d] Typical DTG reaction activity (DME conversion to gasoline-range hydrocarbons with average value at steady-state for DME conversion (X_{DME}) and product distribution) was measured at reaction conditions of T = 290 °C, P = 0.1 MPa, and space velocity (SV) = 4400 L/(kg_{cat}·h) with feed reactant of DME/N_2 = 5/95 (mol%).

The different ZSM-5 morphologies also changed their structural properties. The results of N_2 adsorption–desorption analysis on the various pristine ZSM-5 zeolites are summarized in Table 1, and their isotherms and pore size distributions are, respectively, displayed in Figure 1C and in Supplementary Figure S3B. On N-ZSM-5, the observations of clear increases at P/P_o < 0.15 and P/P_o = 0.4–0.9 suggest the presence of micropores and mesopores due to its nanosized structures, as displayed in Figure 1C. These structural characteristics were also responsible for a larger surface area of 366 m^2/g (196 m^2/g for the external surface area) and a pore volume of 0.29 cm^3/g (0.20 for mesopore volume) with an average pore diameter of 4.1 nm, as summarized in Table 1. H-ZSM-5 exhibited the characteristic H3 hysteresis loop with a sharp increase at P/P_o > 0.9, which was attributed to N_2 adsorption on the inter-particular mesopores formed by the agglomerated larger nanocrystals through the self-assembly of sub-nanocrystal zeolite seeds with CTAB and ethanol [50]. These structural natures also generated larger mesopores with an average

pore size of 7.2 nm and a larger mesopore volume of 0.29 cm^3/g (0.40 cm^3/g for total volume), as well as a larger surface area of 376 m^2/g (177 m^2/g for the external surface area). On S-ZSM-5, the sharp increase at P/P_o = 0.1–0.2 was attributed to a fluid-to-fluid phase transition of the adsorbed N_2 molecules on ZSM-5 having a higher Si/Al ratio due to the capillary condensation effects in ZSM-5 micropores [34,51,52], and no hysteresis loop (type IV) observation at P/P_o = 0.5–0.9 on S-ZSM-5 also suggests the suppressed formation of mesopores in the presence of urea with a smaller surface area of 347 m^2/g and a larger external surface area of 232 m^2/g, as well as a smaller pore volume of 0.10 cm^3/g (0.04 cm^3/g for mesopore volume) and a smaller average pore diameter of 3.9 nm. On C-ZSM-5, these hysteresis loops almost disappeared, and it strongly suggests that the growth of zeolite crystals was limited by preventing the formation of mesopores and developing the much denser crystals with microporous structures, which resulted in a smaller external surface area of 94 m^2/g (360 m^2/g for the specific surface area) and a smaller mesopore volume of 0.10 cm^3/g (0.24 cm^3/g for pore volume) with an average pore diameter of 4.6 nm. It is worth noting that the micropore surface area and micropore volume (differences between the value of total and mesopore) estimated by using the *t*-plot method [53] showed larger variations in the respective values of 115–266 m^2/g and 0.06–0.14 cm^3/g with the largest values on C-ZSM-5 (corresponding to the smaller surface area and pore volume of mesopores), where the larger micropore surface area on C-ZSM-5 was attributed to its higher crystallinity. The larger total surface area and pore volume on N-ZSM-5 and H-ZSM-5 were attributed to their smaller crystallite sizes, and the larger external surface area on S-ZSM-5 originated from the suppressed mesopore formation. In addition, the impregnation of Fe metal oxides on N-ZSM-5 (Fe/N-ZSM-5) also showed H4 hysteresis loop, as shown in Figure 1D, which also suggests the preservation of MFI structures without significant structural disintegrations, as confirmed by PXRD results. As summarized in Table 2, the steady decreases in surface area and pore volume from 366 to 294 m^2/g (196 to 141 m^2/g for the external surface area) and from 0.29 to 0.24 cm^3/g (0.20 to 0.16 cm^3/g for mesopore volume) were observed with an increase in Fe loading up to 15 wt% Fe with the smallest values on Fe(15)/N-ZSM-5, which were also responsible for the steady increases in average pore diameter from 4.1 to 6.0 nm due to the formation of inter-particular mesopores between ZSM-5 and Fe_2O_3 nanoparticles, which suggests that an excess amount of Fe_2O_3 nanoparticles on N-ZSM-5 can further block the outer pore mouths, resulting in suppressed acidic sites as well.

The morphologies of the four different ZSM-5 were further characterized with SEM and TEM analysis, and the images are displayed in Figure 2. The images of the fresh N-ZSM-5, as shown in Figure 2A, clearly revealed the formation of nanosized crystals with an average particle size of 95 nm, where nanocrystalline ZSM-5 showed a rectangular shape with a narrow size distribution. H-ZSM-5, as displayed in Figure 2B, showed bimodal size distributions of the H-ZSM-5 crystallites by selectively forming mesoporous structures with the help of CTAB and ethanol, which caused the formation of hierarchical structures with the growth of smaller crystallites on top of the larger ZSM-5 crystallites with typical MFI morphology [50,54]. S-ZSM-5, as shown in Figure 2C, revealed a typical sheet-like morphology oriented in the direction of the *c*- and *b*-axes, where the addition of urea increased the length along with the *c*-axis due to its preferential crystal growth in the direction of the *b*-axis by inducing the sheet-like morphology of S-ZSM-5 [34,55]. As shown in Figure 2D, C-ZSM-5 exhibited a typical cylindrical cube-like monocrystalline morphology with an average particle size of 300 nm, where dense surfaces and agglomerated nanocrystals were observed on the top of the large ZSM-5 crystallites due to an elevated crystallization temperature of 180 °C.

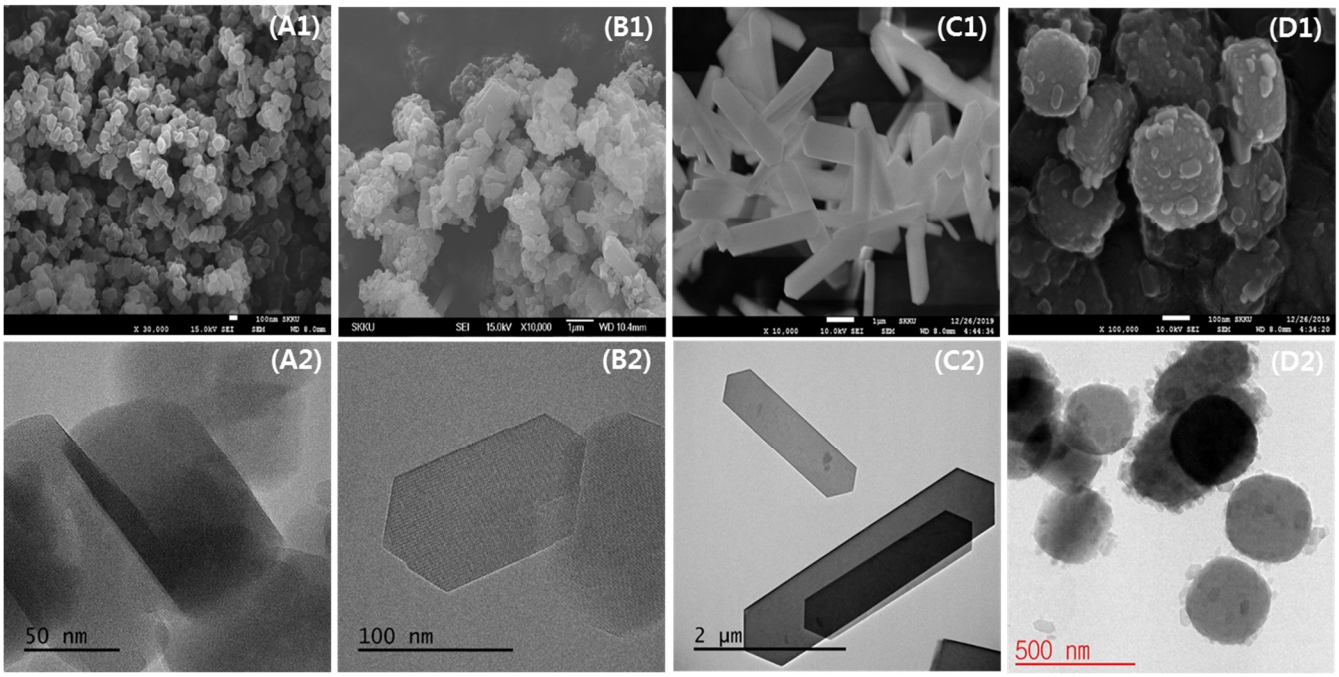

Figure 2. Surface morphology of fresh H-ZSM-5: (**1**) SEM and (**2**) TEM images of (**A**) N-ZSM-5, (**B**) H-ZSM-5, (**C**) S-ZSM-5, and (**D**) C-ZSM-5.

Since the surface acidity can largely change DTG reaction activity and product distributions, NH_3-TPD and FT-IR analyses of adsorbed pyridine on fresh ZSM-5 and Fe/N-ZSM-5 were separately carried out, and the results are, respectively, summarized in Tables 1 and 2, as well as in Figure 3 and Supplementary Figure S4. Three different characteristic NH_3 desorption peaks are assigned to weak (W), medium (M), and strong (S) acid sites at the desorption temperature range of ~150, 250, and 400 °C, respectively (Figure 3A), where two deconvoluted peaks below 250 °C (assigned to weak acid sites) can be separately assigned to the physically absorbed NH_3 and absorbed NH_3 on the weak acidic sites on the zeolite surfaces [56]. The different morphologies of ZSM-5 exhibited different acid site densities in the range of 0.31–0.48 mmol/g with a maximum amount of weak and strong acidic sites of 0.32 and 0.16 mmol/g on N-ZSM-5, whereas S-ZSM-5 showed smaller total and strong acidic sites of 0.31 and 0.12 mmol/g, and the smaller strong acidic sites of 0.13 and 0.06 mmol/g were also observed on C-ZSM-5 and H-ZSM-5 as well (Table 1). Interestingly, S-ZSM-5 having a much smaller mesopore volume (0.04 cm^3/g) and larger external surface area (232 m^2/g) showed much smaller weak acidic sites of 0.19 mmol/g compared to other ZSM-5 in the range of 0.23–0.32 mmol/g, which were attributed to the smaller amount of micropore surface area and the higher Si/Al ratio of 94 of the sheet-like morphology. It was obvious that N-ZSM-5 showed larger amounts of strong Brønsted acid sites (S sites from NH_3-TPD) due to the lower Si/Al ratio of 72 and preferential formation of the bridged–Al(OH)Si- structures in the main zeolite frameworks. In addition, NH_3-TPD analysis was carried out on Fe/N-ZSM-5, and the results are displayed in Figure 3B and summarized in Table 2. All the Fe/N-ZSM-5 zeolites showed very similar NH_3-TPD profiles as pristine N-ZSM-5 with slightly suppressed amounts of weak and strong acid sites. With an increase in Fe content on N-ZSM-5, the amount of weak and strong acidic sites steadily decreased from 0.32 and 0.16 mmol/g on N-ZSM-5 (total acidic sites of 0.48 mmol/g) to 0.18 and 0.10 mmol/g (total acidic sites of 0.27 mmol/g) on Fe(15)/N-ZSM-5, which were mainly attributed to the selective blockages of active sites by the excessive amount of Fe_2O_3 nanoparticles, as confirmed by XRD analysis. To further verify the types and amounts of surface acidic sites, Py-IR analysis was performed on the different ZSM-5 zeolites, and the results are displayed in Figure 3C and summarized in Table 1. Typically,

the absorption band at 1540 cm^{-1} is responsible for its adsorption on the Brønsted acid sites, and the band at 1455 cm^{-1} is mainly assigned to the Lewis acid sites formed by extra framework Al (EFAL) sites. It is well reported that the strong Brønsted acid sites such as the bridged Si–OH–Al groups on ZSM-5 play important roles in the propagation reaction, alkene dehydrogenation, and cyclization to aromatics [48,57]. The distributions of Brønsted (B) and Lewis (L) acid sites were measured by calculating each peak ratio (B/L) from the Py-IR spectra at a desorption temperature of 350 °C (close to the real reaction temperature), where the much smaller and clear peaks at 350 °C were observed compared to the desorption temperatures of 150 and 250 °C, as shown in Supplementary Figure S4. The relative B/L ratios were found in the decreasing order of N-ZSM-5 > C-ZSM-5 > H-ZSM-5 > S-ZSM-5 with respective values of 32.2, 20.7, 25.5, and 11.4 (density of Brønsted acid sites in the range of 48.4–159.9 μmol/g and Lewis acid sites in the range of 4.1–5.4 μmol/g). Interestingly, N-ZSM-5 exhibited the largest B/L ratio due to the abundant Brønsted acid sites compared to other ZSM-5. These different distributions of Brønsted and Lewis acid sites according to the different morphologies of ZSM-5 and amounts of Fe promoter on N-ZSM-5 seem to largely alter DME conversion and product distributions as well.

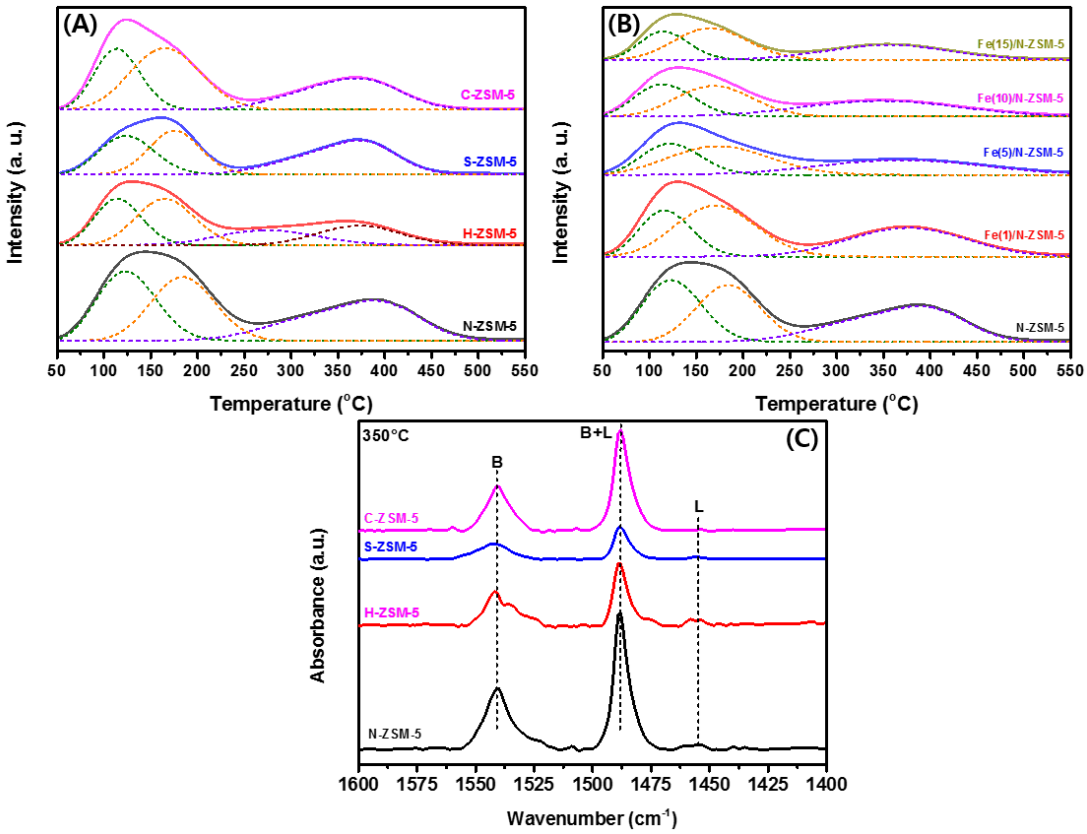

Figure 3. NH_3-TPD patterns of fresh (**A**) ZSM-5 and (**B**) Fe/N-ZSM-5 and (**C**) Py-IR spectra of ZSM-5.

2.2. Catalytic Activity and Product Distribution According to ZSM-5 Morphology

The catalytic activity of the DTG reaction was measured at the temperature range of 280–320 °C on the different ZSM-5 zeolites to verify the roles of the different morphologies and acidic site densities, and DME conversion and hydrocarbon distributions are summarized in Table 1 (at 290 °C and at a wider range of temperatures in Supplementary Table S1) and displayed in Figure 4. All ZSM-5 zeolites showed almost 100% DME conversion on all tested temperature ranges, and the selectivity to gaseous C_1–C_4 hydrocarbons steadily increased with an increase in reaction temperature, for example, from its selectivity of 33.1% at 280 °C to 39.3% at 320 °C on N-ZSM-5 and from 37.9–42.8% to 48.3–48.4% on C-ZSM-5 and S-ZSM-5 (Table S1), which was attributed to the facile cracking activity of surface

intermediates to form light hydrocarbons. Among the different ZSM-5 zeolites, N-ZSM-5 showed a much higher selectivity to gasoline-range hydrocarbons (C_{5+} selectivity of 41.7% with aromatic selectivity of 23.6% at 290 °C) with lower light hydrocarbon selectivity. These phenomena were mainly attributed to the largest amount of strong Brønsted acid sites with a higher B/L ratio, as confirmed by NH_3-TPD and Py-IR results. The strong Brøsnted acid sites have been generally known to be more active in enhancing C–C bond formations, which further transform to form heavier hydrocarbons [58,59]. The largest amounts of total acidic sites are also responsible for the higher gasoline-range hydrocarbon selectivity on N-ZSM-5 due to its shorter diffusion pathlength in the smaller crystallites with lower cracking reaction activity of intermediates [60]. However, S-ZSM-5 having larger crystallite sizes and smaller acidic sites exhibited a higher selectivity to C_1–C_4 hydrocarbons with 43.4% and the smaller formation of C_{5+} and aromatics hydrocarbons with 38.1 and 18.5%, respectively. These phenomena were attributed to the smallest amount of strong Brønsted acid sites by suppressing chain propagation reactions to form gasoline-range aliphatic hydrocarbons [61]. In addition, H-ZSM-5 possessing smaller aggregates on the MFI morphology increased the mass transfer rate and minimized coke formations due to the presence of the hierarchically structured morphology of H-ZSM-5 [9,62,63], which was responsible for a higher C_{5+} selectivity of 41.0% and aromatics selectivity of 21.9% with a lower C_1–C_4 selectivity of 37.1%. C-ZSM-5 having a similar amount of Brøsnted and total acid sites with N-ZSM-5 and a higher content of total acid sites showed a higher selectivity to the gaseous C_1–C_4 hydrocarbons of 39.5% due to the presence of more active cylindrical cube-like densely agglomerated nanocrystals.

In addition, the catalytic activity of Fe/N-ZSM-5 with different Fe contents was measured at 290 °C, which showed the synergy effects of the proper amount of Fe_2O_3 promoter on the most active N-ZSM-5 by increasing the selectivity of C_{6+} hydrocarbons with 69.6% (aromatics selectivity of 17.6%) on Fe(10)/N-ZSM-5, as displayed in Figure 5A and summarized in Table 2 and Supplementary Table S2. On all the Fe/N-ZSM-5 zeolites, DME conversion was found to be ~100%, except for Fe(15)/N-ZSM-5 with 83.5%, and the aromatics selectivity gradually decreased with an increase in Fe_2O_3 content from 23.6% on pristine N-ZSM-5 to 17.0% on Fe(15)/N-ZSM-5 with an increased liquid-phase aliphatic selectivity from 63.8 to 70.9% (Table S2) due to decreased amounts of strong Brøsnted acid sites, which also originated from the possible secondary hydrogenation and isomerization reaction to form aromatics with the presence of Fe_2O_3 nanoparticles on N-ZSM-5 [41,42], as shown in Figure 5B. The surface modification with Fe_2O_3 phases also increased the selectivity to C_1–C_4 light hydrocarbons from 34.7% on N-ZSM-5 to 44.5% on Fe(15)/N-ZSM-5 possessing a larger average Fe_2O_3 size of 13.6 nm, except for Fe(10)/N-ZSM-5 with a selectivity of 21.9%, as summarized in Table 2. Therefore, the amount of strong Brønsted acid sites seems to be closely related to the aromatization reaction over ZSM-5 surfaces, and incorporation with a proper amount of Fe_2O_3 can further optimize the surface Brønsted acid sites [42] through the homogeneous distribution of Fe nanoparticles. Fe(10)/N-ZSM-5 exhibited the lowest C_1–C_4 light hydrocarbon selectivity of 21.9% and the highest selectivity to gasoline-range hydrocarbons of 69.6%. The results were attributed to the presence of an optimal amount of strong Brønsted acid sites, as well as well-dispersed Fe_2O_3 nanoparticles with an average Fe_2O_3 size of 11.1 nm by weakening the cracking reaction activity of N-ZSM-5, where the optimal Fe_2O_3 crystallite size of ~10 nm seems to properly adjust the surface acidic sites without significant blockages of the active sites [64,65]. The more detailed reaction mechanisms for DME conversion to gasoline-range hydrocarbons by stepwise surface methoxy formation, alkylation, hydrogen transfer, and aromatization [14] were modified and are displayed in Supplementary Figure S5. As a brief summary, nanostructured N-ZSM-5 possessing abundant strong Brønsted acid sites can be one of the promising catalyst candidates for a gas-phase methanol/DTG reaction with higher gasoline-range hydrocarbon selectivity, which can be further optimized with a proper amount of Fe_2O_3 nanoparticles (10 wt% Fe on N-ZSM-5) by modifying the surface

acidic sites with the suppressed cracking reaction activity of the surface intermediates as well.

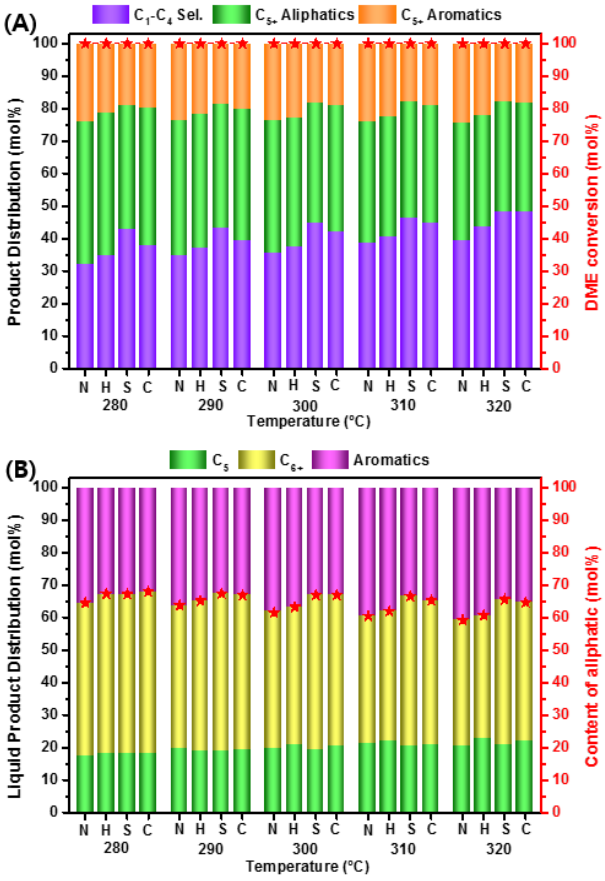

Figure 4. Catalytic activity and product distribution on four different ZSM-5 zeolites (N for N-ZSM-5, H for H-ZSM-5, S for S-ZSM-5, and C for C-ZSM-5) at reaction temperature of 280–320 °C, P = 0.1 MPa, DME/N_2 (mol%) = 5/95, and weight hourly space velocity (SV) = 4400 L/(kg_{cat}·h) with catalyst loading of 0.4 g; (**A**) DME conversion and total selectivity of C_1–C_4 and C_{5+} hydrocarbons and (**B**) liquid hydrocarbon distributions above C_{5+} hydrocarbons.

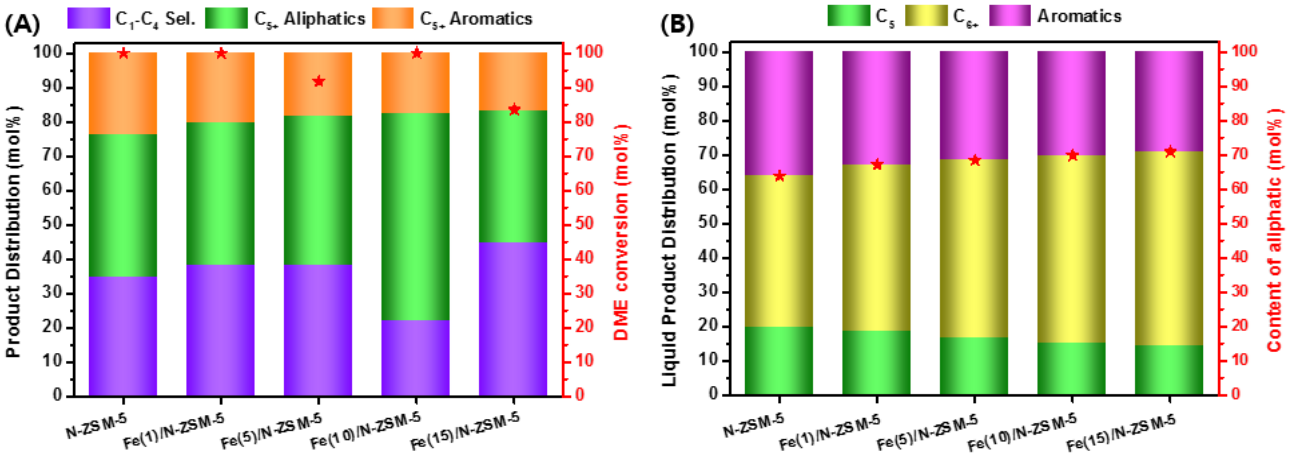

Figure 5. Catalytic activity and product distribution on Fe/N-ZSM-5: (**A**) DME conversion and selectivity of C_1–C_4 and C_{5+} hydrocarbons and (**B**) liquid hydrocarbon distributions above C_{5+} hydrocarbons at reaction condition of T = 290 °C, P = 0.1 MPa, DME/N_2 (mol%) = 5/95, and weight hourly space velocity (SV) = 4400 L/(kg_{cat}·h) with catalyst loading of 0.4 g.

3. Experimental Section

3.1. Catalyst Preparations and Activity Measurement

The ZSM-5 (Si/Al ratio of ~80) zeolite with different morphologies was synthesized by a typical synthetic method, as more precisely described in the Supplementary Materials. Briefly, the synthesis of nanostructured ZSM-5 (N-ZSM-5) and hierarchically structured nano-ZSM-5 (H-ZSM-5) was carried out with silicalite-1 seed suspension, and the silicalite-1 seed suspension was prepared by mixing tetraethyl orthosilicate (TEOS), tetrapropyl ammonium hydroxide (TPAOH), and deionized water (DIW) in a Teflon-lined stainless steel autoclave at 80 °C for 72 h. For the synthesis of N-ZSM-5, the $Al_2(SO_4)_3 \cdot 18H_2O$ precursor was dissolved in DIW, followed by the addition of ammonium hydroxide, and the mixture was stirred for several minutes before adding the deionized colloidal silica (Ludox TMA) and silicalite-1 seed. For the synthesis of H-ZSM-5, the mixture was added with cetyltrimethylammonium bromide (CTAB) and ethanol. Then, the solution was stirred for 1 h at room temperature and transferred into a Teflon-lined stainless steel autoclave for further crystallization. N-ZSM-5 was treated by heating at 175 °C for 24 h, and H-ZSM-5 was treated at 150 °C for 60 h. Subsequently, the white-colored solid powders were then collected with additional water and separated and washed with DIW until the pH approached 7. Then, the obtained powders were dried overnight at 110 °C and calcined at 550 °C for 7 h at a ramp rate of 2 °C/min to obtain H-form ZSM-5.

Furthermore, conventional ZSM-5 (C-ZSM-5) was prepared by a hydrothermal synthesis method with the molar composition of ($2TEOS/0.68TPAOH/8ethanol/120H_2O/xAl_2O_3$). The mixture was prepared by adding DIW and ethanol to TPAOH. After its complete mixing, aluminum isopropoxide (AIP) was added as an Al source; finally, TEOS as a Si source was added dropwise, and the solution was stirred overnight, whereas for the synthesis of sheet-like ZSM-5 (S-ZSM-5) after the addition of TEOS, urea was added to the above solution and aged overnight. In addition, the solution was sealed in an autoclave and heated to 180 °C for 24 h for the C-ZSM-5 preparation and treated at 180 °C for 48 h for S-ZSM-5 at a rotation speed of 5 rpm. After the crystallization step, the white powders were collected, and the mother solution was washed with deionized water until the solution pH approached 7, then the sample was dried overnight at 110 °C. Finally, H-form ZSM-5 zeolite was obtained after calcination at 550 °C for 6 h at a heating rate of 1 °C/min. To prepare Fe-modified N-ZSM-5 (Fe/N-ZSM-5), H-form ZSM-5 was impregnated with $Fe(NO_3)_3 \cdot 9H_2O$ solution, and the resulting mixture was evaporated at 80 °C. Then, the white powder was dried at 110 °C and calcined at 550 °C for 5 h. Finally, the obtained catalysts were denoted as Fe(x)/N-ZSM-5, where x represents wt% of Fe loading in the range of 0–15 wt%.

Conversion of DME to gasoline-range hydrocarbons (DTG) reaction was carried out to elucidate the roles of the different morphologies of ZSM-5 and Fe promoters on N-ZSM-5. A fixed-bed tubular reactor was loaded with 0.4 g of catalyst, and it was pretreated under a flow of N_2 at 500 °C for 2 h. The DTG reaction was carried out in the temperature range of 280–320 °C with 10 °C intervals for each 10 h reaction period at a weight hourly space velocity (SV) of 4400 $L/(kg_{cat} \cdot h)$ with a feed gas composition of DME/N_2 (mol%) = 5/95 under ambient pressure, and the schematic diagram of the catalytic reaction system is displayed in Supplementary Figure S1. DME conversion and product distributions were analyzed by using online gas chromatography (YL 6500 GC, YOUNG IN Chromass, Gyeonggi-do, Korea) equipped with a flame ionization detector (FID) and connected with a DB-Petro capillary column to analyze gaseous and liquid hydrocarbons. One typical GC spectra of gas-phase products and analysis conditions of GC are also displayed in Supplementary Figure S2. DME conversion and hydrocarbon distributions were calculated based on total carbon balance by using the equations explained in the Supplementary Materials.

3.2. Catalyst Characterization

Powder X-ray diffraction (PXRD) analysis was performed with an X'Pert PRO Multipurpose X-ray Diffractometer (PANalytical, Malvern, UK) by using Cu Kα radiation (λ = 0.154 nm) operated at 60 kV and 55 mA to determine crystalline phases of fresh ZSM-5 at a scanning rate of 4°/min in the range of 5–90°. The average crystallite sizes of ZSM-5 were calculated by using a Debye–Sherrer equation. A Tristar II 3020 instrument (Micromeritics, GA, USA) was used for N_2 adsorption–desorption analysis at −196 °C with a Brunauer–Emmett–Teller (BET) model to calculate a specific surface area (Sg, m^2/g) and by using a Barrett–Joyner–Halenda (BJH) model to determine the average pore diameter (P_D, nm) and pore volume (Pv, cm^3/g). Prior to the analysis, the ZSM-5 zeolite was degassed at 90 °C for 1 h, followed by 350 °C for 4 h. X-ray fluorescence (XRF) analysis by using an S8 Tiger (Bruker, MA, USA) instrument operated at 60 kVm and 50–170 mA was used to verify the bulk Si/Al ratio of ZSM-5 zeolites. The different surface morphologies of ZSM-5 were observed by using scanning electron microscopy (SEM) with a JSM7500F instrument (JEOL, Tokyo, Japan) operated at 30 kV acceleration voltage. Transmission electron microscopy (TEM) images were also obtained by using a JEM ARM 200F (JEOL Tokyo, Japan) instrument operated at 200 kV.

Temperature-programmed desorption of NH_3 (NH_3-TPD) analysis was performed by using a BELCAT-M(MICROTRAC MRB, PA, USA) instrument. Before the analysis, ~50 mg of ZSM-5 was heated under He flow with 50 mL/min at 500 °C for 1 h. After the pretreatment, the sample was exposed to 10%NH_3/Ar gas at 50 °C for 1 h at a flow rate of 50 mL/min, and the physically absorbed NH_3 was purged out under He flow. Finally, NH_3 TPD analysis was subsequently performed in the temperature range of 100–800 °C at a ramping rate of 10 °C/min. Furthermore, to identify the surface acid sites and types such as Brønsted and Lewis acid sites, FT-IR of the adsorbed pyridine (Py-IR) analysis was performed by using a Perkin Elmer Spectrum 2000 spectrometer (Perkin Elmer, MA, USA) in the wavenumber range of 1300–4000 cm^{-1} at the resolution of 4 cm^{-1}. Typically, ~20 mg of ZSM-5 was pressed to a self-supported wafer, and it was pretreated at 350 °C for 1 h under a vacuum condition. Subsequently, the pyridine probe molecules were adsorbed at 150 °C for 1 h, and the physisorbed pyridine molecules were desorbed for 30 min under vacuum conditions. FT-IR spectra including background spectra were collected at each desorption temperature of 350, 250 and 150 °C.

4. Conclusions

Four distinctively different morphologies of ZSM-5 such as rectangular, hexagonal, sheet-like, and sphere-type and Fe modified N-ZSM-5 were investigated to elucidate the synergistic effects of Fe_2O_3 phases for dimethyl ether (DME) conversion to the gasoline-range hydrocarbon (DTG) reaction. Nanostructured N-ZSM-5 showed the highest C_{5+} selectivity of 41.7% with a higher aromatics selectivity of 23.6% and a lower selectivity of C_1–C_4 hydrocarbons with 34.7% at ~100% DME conversion. The smaller crystallite sizes on N-ZSM-5 with typical rectangular morphology revealed higher total and Brønsted acid sites, which facilitates the formation of heavier C_{5+} hydrocarbons with smaller cracking reaction activity through a faster transfer rate of products due to their shorter diffusion pathlength on N-ZSM-5. In addition, Fe(10)/N-ZSM-5 showed enhanced C_{5+} selectivity with a smaller light hydrocarbon selectivity of 21.9%, which was also attributed to the adjusted acidic sites by suppressing the cracking reaction activity of the surface intermediates to prevent smaller hydrocarbon formation. Nanostructured N-ZSM-5 with a larger amount of Brønsted acid sites with a well-dispersed Fe_2O_3 promoter revealed a higher formation rate of gasoline-range hydrocarbons due to the enhanced secondary reactions of intermediates to form heavier hydrocarbons.

Supplementary Materials: The following supporting information can be downloaded at https://www.mdpi.com/article/10.3390/catal13050910/s1, Figure S1: Schematic diagram of catalytic activity measurement system, Figure S2: (A) Original chromatograph peaks of the measurable products and

(B) Temperature-program for GC analysis, Figure S3: PXRD patterns; (A) PXRD patterns of the fresh ZSM-5 in the range of (1) 2θ = 7–10°, (2) 2θ = 22.5–25.0°, (B) Pore size distribution of the fresh ZSM-5 and (C) Pore size distribution of the fresh Fe/N-ZSM-5., Figure S4: FT-IR spectra of the adsorbed pyridine (Py-IR) at two different desorption temperatures of (A) 150 °C and (2) 250 °C on the fresh ZSM-5., Figure S5: Proposed reaction pathways for DTG over HZSM-5 catalyst, where the labels over arrows represents each reaction step, Table S1: Catalytic activity for DME conversion to gasoline-range hydrocarbons (mol%) on ZSM-5 catalysts with their different morphology, Table S2: Catalytic activity for DME conversion to gasoline-range hydrocarbons (mol%) on Fe/N-ZSM-5 catalysts [14].

Author Contributions: Methodology, M.A.; formal analysis, J.J.K. and X.W.; data curation, F.Z. and D.S.; writing—original draft preparation, M.A. and J.W.B.; writing—review and editing, J.W.B.; supervision, J.W.B.; funding acquisition, J.W.B. All authors have read and agreed to the published version of the manuscript.

Funding: The funding data for this research were mentioned in acknowledgment section.

Data Availability Statement: Data is contained within the article or supplementary material.

Acknowledgments: The authors would sincerely like to acknowledge financial support from the National Research Foundation of Korea (NRF) grant funded by the South Korea government (NRF-2018M3D3A1A01018009). This work was supported by the Korea Institute of Technology (KIAT) and the Ministry of Trade, Industry and Energy (MOTIE) of the Republic of Korea (No. P0017363).

Conflicts of Interest: The authors declare no conflict of interest.

References

1. Walsh, B.; Ciais, P.; Janssens, I.A.; Penuelas, J.; Riahi, K.; Rydzak, F.; Van Vuuren, D.P.; Obersteiner, M. Pathways for balancing CO_2 emissions and sinks. *Nat. Commun.* **2017**, *8*, 14856. [CrossRef]
2. Sun, J.; Yang, G.; Yoneyama, Y.; Tsubaki, N. Catalysis chemistry of dimethyl ether synthesis. *ACS Catal.* **2014**, *4*, 3346–3356.
3. Tian, P.; Wei, Y.; Ye, M.; Liu, Z. Methanol to olefins (MTO): From fundamentals to commercialization. *ACS Catal.* **2015**, *5*, 1922–1938.
4. Nielsen, N.D.; Jensen, A.D.; Christensen, J.M. The roles of CO and CO_2 in high pressure methanol synthesis over Cu-based catalysts. *J. Catal.* **2021**, *393*, 324–334.
5. Palčić, A.; Jaén, S.N.; Wu, D.; Cai, M.; Liu, C.; Pidko, E.A.; Khodakov, A.Y.; Ordomsky, V.; Valtchev, V. Embryonic zeolites for highly efficient synthesis of dimethyl ether from syngas. *Microporous Mesoporous Mater.* **2011**, *322*, 111138. [CrossRef]
6. Peláez, R.; Marín, P.; Ordóñez, S. Direct synthesis of dimethyl ether from syngas over mechanical mixtures of $CuO/ZnO/Al_2O_3$ and γ-Al_2O_3: Process optimization and kinetic modelling. *Fuel Process. Technol.* **2017**, *168*, 40–49. [CrossRef]
7. Pelaez, R.; Bryce, E.; Marin, P.; Ordonez, S. Catalyst deactivation in the direct synthesis of dimethyl ether from syngas over $CuO/ZnO/Al_2O_3$ and γ-Al_2O_3 mechanical mixtures. *Fuel Process. Technol.* **2018**, *179*, 378–386.
8. Sun, Y.; Han, X.; Zhao, Z. Direct coating copper-zinc-aluminum oxalate with H-ZSM-5 to fabricate a highly efficient capsule-structured bifunctional catalyst for dimethyl ether production from syngas. *Catal. Sci. Technol.* **2019**, *9*, 3763–3770.
9. Su, X.; Zhang, K.; Snatenkova, Y.; Matieva, Z.; Bai, X.; Kolesnichenko, N.; Wu, W. High-efficiency nano [Zn, Al] ZSM-5 bifunctional catalysts for dimethyl ether conversion to isoparaffin-rich gasoline. *Fuel Process. Technol.* **2020**, *198*, 106242. [CrossRef]
10. Wen, Z.; Li, Z.; Ge, Q.; Zhou, Y.; Sun, J.; Abroshan, H.; Li, G. Robust nickel cluster@ Mes-HZSM-5 composite nanostructure with enhanced catalytic activity in the DTG reaction. *J. Catal.* **2018**, *363*, 26–33.
11. Tan, E.C.; Talmadge, M.; Dutta, A.; Hensley, J.; Snowden-Swan, L.J.; Humbird, D.; Schaidle, J.; Biddy, M. Conceptual process design and economics for the production of high-octane gasoline blendstock via indirect liquefaction of biomass through methanol/dimethyl ether intermediates. *Biofuel. Bioprod. Bioref.* **2016**, *10*, 17–35. [CrossRef]
12. Haro, P.; Trippe, F.; Stahl, R.; Henrich, E. Bio-syngas to gasoline and olefins via DME-A comprehensive techno-economic assessment. *Appl. Energy* **2013**, *108*, 54–65. [CrossRef]
13. Ilias, S.; Bhan, A. Mechanism of the Catalytic Conversion of Methanol to Hydrocarbons. *ACS Catal.* **2013**, *3*, 18–31. [CrossRef]
14. Lee, D.; Kim, J.J.; Ali, M.; Choung, J.W.; Lee, W.B.; Bae, J.W.; Park, M.J. Mechanistic kinetic modeling for catalytic conversion of DME to gasoline-range hydrocarbons over nanostructured ZSM-5. *Catal. Sci. Technol.* **2022**, *12*, 4798–4810. [CrossRef]
15. Primo, A.; Garcia, H. Zeolites as catalysts in oil refining. *Chem. Soc. Rev.* **2014**, *43*, 7548–7561. [CrossRef]
16. Kokotailo, G.T.; Lawton, S.L.; Olson, D.H.; Meier, W.M. Structure of synthetic zeolite ZSM-5. *Nature* **1978**, *272*, 437–438. [CrossRef]
17. Li, J.; Wei, Y.; Liu, G.; Qi, Y.; Tian, P.; Li, B.; He, Y.; Liu, Z. Comparative study of MTO conversion over SAPO-34, H-ZSM-5 and H-ZSM-22: Correlating catalytic performance and reaction mechanism to zeolite topology. *Catal. Today* **2011**, *171*, 221–228. [CrossRef]
18. Maximov, A.; Magomedova, M.; Galanova, E.; Afokin, M.; Ionin, D. Primary and secondary reactions in the synthesis of hydrocarbons from dimethyl ether over a Pd-Zn-HZSM-5/Al_2O_3 catalyst. *Fuel Process. Technol.* **2020**, *199*, 106281. [CrossRef]

19. Gao, P.; Xu, J.; Qi, G.; Wang, C.; Wang, Q.; Zhao, Y.; Zhang, Y.; Feng, N.; Zhao, X.; Li, J.; et al. A mechanistic study of methanol-to-aromatics reaction over Ga-modified ZSM-5 zeolites: Understanding the dehydrogenation process. *ACS Catal.* **2018**, *8*, 9809–9820. [CrossRef]
20. Shoinkhorova, T.; Dikhtiarenko, A.; Ramirez, A.; Chowdhury, A.D.; Caglayan, M.; Vittenet, J.; Bendjeriou-Sedjerari, A.; Ali, O.S.; Morales-Osorio, I.; Xu, W.; et al. Shaping of ZSM-5-based catalysts via spray drying: Effect on methanol-to-olefins performance. *ACS Appl Mater. Inter.* **2019**, *11*, 44133–44143. [CrossRef]
21. Jin, W.Y.; Qiao, J.R.; Yu, J.P.; Wang, Y.L.; Cao, J.P. Influence of hollow ZSM-5 zeolites prepared by treatment with different alkalis on the catalytic conversion of methanol to aromatics. *Energy Fuels* **2020**, *34*, 14633–14646. [CrossRef]
22. Li, J.; Liu, M.; Guo, X.; Xu, S.; Wei, Y.; Liu, Z.; Song, C. Interconnected hierarchical ZSM-5 with tunable acidity prepared by a dealumination–realumination process: A superior MTP catalyst. *ACS Appl. Mater. Inter.* **2017**, *9*, 26096–26106. [CrossRef]
23. Kunz, J.; Kraushaar-Czarnetzki, B. Dynamic processing of dimethyl ether and methanol to gasoline (DMTG): Investigation of kinetic transitions at fluctuating workloads under isothermal conditions. *Chem. Eng. J.* **2019**, *373*, 1295–1308. [CrossRef]
24. Young, L.B.; Butter, S.A.; Kaeding, W.W. Shape selective reactions with zeolite catalysts: III. Selectivity in xylene isomerization, toluene-methanol alkylation, and toluene disproportionation over ZSM-5 zeolite catalysts. *J. Catal.* **1982**, *76*, 418–432. [CrossRef]
25. Fraenkel, D.; Cherniavsky, M.; Ittah, B.; Levy, M. Shape-selective alkylation of naphthalene and methylnaphthalene with methanol over H-ZSM-5 zeolite catalysts. *J. Catal.* **1986**, *101*, 273–283. [CrossRef]
26. Chen, N.Y.; Ketkar, A.B.; Partridge, R.D. Mobil Oil Corporation, New York. Integrated Catalytic Dewaxing and Catalytic Cracking Process. U.S. Patent 4,944,862, 31 July 1990.
27. Kuo, J.C.; Prater, C.H.; Wise, J.J. Mobil Oil Corporation, New York. Method for Upgrading Fischer-Tropsch Synthesis Products. U.S. Patent 4,049,741, 20 September 1977.
28. Wang, T.; Yang, C.; Gao, P.; Zhou, S.; Li, S.; Wang, H.; Sun, Y. ZnZrOx integrated with chain-like nanocrystal HZSM-5 as efficient catalysts for aromatics synthesis from CO_2 hydrogenation. *Appl. Catal. B-Environ.* **2021**, *286*, 119929. [CrossRef]
29. Zhang, Q.; Yu, J.; Corma, A. Applications of zeolites to C1 chemistry: Recent advances, challenges, and opportunities. *Adv. Mater.* **2020**, *32*, 2002927. [CrossRef] [PubMed]
30. Łukaszuk, K.A.; Rojo-Gama, D.; Øien-Ødegaard, S.; Lazzarini, A.; Berlier, G.; Bordiga, S.; Lillerud, K.P.; Olsbye, U.; Beato, P.; Lundegaard, L.F.; et al. Zeolite morphology and catalyst performance: Conversion of methanol to hydrocarbons over offretite. *Catal. Sci. Technol.* **2017**, *7*, 5435–5447. [CrossRef]
31. Wang, K.; Dong, M.; Niu, X.; Li, J.; Qin, Z.; Fan, W.; Wang, J. Highly active and stable Zn/ZSM-5 zeolite catalyst for the conversion of methanol to aromatics: Effect of support morphology. *Catal. Sci. Technol.* **2018**, *8*, 5646–5656. [CrossRef]
32. Fu, T.; Zhou, H.; Li, Z. Effect of particle morphology for ZSM-5 zeolite on the catalytic conversion of methanol to gasoline-range hydrocarbons. *Catal. Lett.* **2016**, *146*, 1973–1983. [CrossRef]
33. Wen, C.; Wang, C.; Chen, L.; Zhang, X.; Liu, Q.; Ma, L. Effect of hierarchical ZSM-5 zeolite support on direct transformation from syngas to aromatics over the iron-based catalyst. *Fuel* **2019**, *244*, 492–498. [CrossRef]
34. Yang, J.; Gong, K.; Miao, D.; Jiao, F.; Pan, X.; Meng, X.; Xiao, F.; Bao, X. Enhanced aromatic selectivity by the sheet-like ZSM-5 in syngas conversion. *J. Energy Chem.* **2019**, *35*, 44–48. [CrossRef]
35. Ni, Y.; Sun, A.; Wu, X.; Hai, G.; Hu, J.; Li, T.; Li, G. The preparation of nano-sized H [Zn, Al] ZSM-5 zeolite and its application in the aromatization of methanol. *Microporous Mesoporous Mater.* **2011**, *143*, 435–442. [CrossRef]
36. Freeman, D.; Wells, R.P.K.; Hutchings, G.J. Conversion of methanol to hydrocarbons over Ga_2O_3/H-ZSM-5 and Ga_2O_3/WO_3 catalysts. *J. Catal.* **2002**, *205*, 358–365. [CrossRef]
37. Hajjar, Z.; Khodadadi, A.; Mortazavi, Y.; Tayyebi, S.; Soltanali, S. Artificial intelligence modeling of DME conversion to gasoline and light olefins over modified nano ZSM-5 catalysts. *Fuel* **2016**, *179*, 79–86. [CrossRef]
38. Zhang, Q.; Tan, Y.; Yang, C.; Xie, H.; Han, Y. Characterization and catalytic application of $MnCl_2$ modified HZSM-5 zeolites in synthesis of aromatics from syngas via dimethyl ether. *J. Ind. Eng. Chem.* **2013**, *19*, 975–980. [CrossRef]
39. Kecskeméti, A.; Barthos, R.; Solymosi, F. Aromatization of dimethyl and diethyl ethers on Mo_2C-promoted ZSM-5 catalysts. *J. Catal.* **2018**, *258*, 111–120. [CrossRef]
40. Golubev, K.B.; Zhang, K.; Su, X.; Kolesnichenko, N.V.; Wu, W. Dimethyl ether aromatization over nanosized zeolites: Effect of preparation method and zinc modification on catalyst performance. *Catal. Commun.* **2021**, *149*, 106176. [CrossRef]
41. Xu, Y.; Liu, J.; Ma, G.; Wang, J.; Lin, J.; Wang, H.; Zhang, C.; Ding, M. Effect of iron loading on acidity and performance of Fe/HZSM-5 catalyst for direct synthesis of aromatics from syngas. *Fuel* **2018**, *228*, 1–9. [CrossRef]
42. Li, J.; Miao, P.; Li, Z.; He, T.; Han, D.; Wu, J.; Wang, Z.; Wu, J. Hydrothermal synthesis of nanocrystalline H [Fe, Al] ZSM-5 zeolites for conversion of methanol to gasoline. *Energy Convers. Manag.* **2015**, *93*, 259–266. [CrossRef]
43. Gu, Y.; Chen, P.; Wang, X.; Lyu, Y.; Liu, W.; Liu, X.; Yan, Z. Active sites and induction period of Fe/ZSM-5 catalyst in methane dehydroaromatization. *ACS Catal.* **2021**, *11*, 6771–6786. [CrossRef]
44. Li, J.; Han, D.; He, T.; Liu, G.; Zi, Z.; Wang, Z.; Wu, J.; Wu, J. Nanocrystal H [Fe, Al] ZSM-5 zeolites with different silica-alumina composition for conversion of dimethyl ether to gasoline. *Fuel Process. Technol.* **2019**, *191*, 104–110. [CrossRef]
45. Li, J.; Han, D.; Zi, Z.; He, T.; Liu, G.; Wang, Z.; Wu, J.; Wu, J. The synthesis of H [Fe, Al] ZSM-5 zeolites with uniform nanocrystals for dimethyl ether to gasoline reaction. *Fuel* **2022**, *313*, 122643. [CrossRef]
46. Jamil, A.K.; Muraza, O.; Miyake, K.; Ahmed, M.H.M.; Yamani, Z.H.; Hirota, Y.; Nishiyama, N. Stable production of gasoline-ranged hydrocarbons from dimethyl ether over iron-modified ZSM-22 zeolite. *Energy Fuels* **2018**, *32*, 11796–11801. [CrossRef]

47. LaFollette, M.R.; Lobo, R.F. Olefin methylation over iron zeolites and the methanol to hydrocarbons reaction. *Appl. Catal. A Gen.* **2022**, *641*, 118645. [CrossRef]
48. Wei, J.; Yao, R.; Ge, Q.; Xu, D.; Fang, C.; Zhang, J.; Xu, H.; Sun, J. Precisely regulating Brønsted acid sites to promote the synthesis of light aromatics via CO_2 hydrogenation. *Appl. Catal. B-Environ.* **2021**, *283*, 119648. [CrossRef]
49. Wu, W.; Hao, R.; Liu, F.; Su, X.; Hou, Y. Single-crystalline α-Fe_2O_3 nanostructures: Controlled synthesis and high-index plane-enhanced photodegradation by visible light. *J. Mater. Chem. A* **2013**, *1*, 6888–6894. [CrossRef]
50. Zhu, Y.; Hua, Z.; Zhou, J.; Wang, L.; Zhao, J.; Gong, Y.; Wu, W.; Ruan, M.; Shi, J. Hierarchical mesoporous zeolites: Direct self-assembly synthesis in a conventional surfactant solution by kinetic control over the zeolite seed formation. *Chem. Eur. J.* **2011**, *17*, 14618–14627. [CrossRef]
51. Jin, D.; Ye, G.; Zheng, J.; Yang, W.; Zhu, K.; Coppens, M.-O.; Zhou, X. Hierarchical silicoaluminophosphate catalysts with enhanced hydroisomerization selectivity by directing the orientated assembly of premanufactured building blocks. *ACS Catal.* **2017**, *7*, 5887–5902. [CrossRef]
52. Groen, J.C.; Peffer, L.A.A.; Pérez-Ramırez, J. Pore size determination in modified micro-and mesoporous materials. Pitfalls and limitations in gas adsorption data analysis. *Microporous Mesoporous Mater.* **2003**, *60*, 1–17. [CrossRef]
53. Sing, K.S.W. Physisorption of nitrogen by porous materials. *J. Porous Mater.* **1995**, *2*, 5–8. [CrossRef]
54. Beerthuis, R.; Huang, L.; Shiju, N.R.; Rothenberg, G.; Shen, W.; Xu, H. Facile synthesis of a novel hierarchical ZSM-5 zeolite: A stable acid catalyst for dehydrating glycerol to acrolein. *ChemCatChem* **2018**, *10*, 211. [CrossRef] [PubMed]
55. Liu, Z.; Wu, D.; Ren, S.; Chen, X.; Qiu, M.; Wu, X.; Yang, C.; Zeng, G.; Sun, Y. Solvent-free synthesis of c-axis oriented ZSM-5 crystals with enhanced methanol to gasoline catalytic activity. *ChemCatChem* **2016**, *8*, 3317–3322. [CrossRef]
56. Ali, M.; Koo, H.-M.; Kasipandi, S.; Han, G.Y.; Bae, J.W. Direct synthesis of liquid fuels and aromatics from syngas over mesoporous FeZrOx catalyst mixed with Mo/ferrierite. *Fuel* **2020**, *264*, 116851. [CrossRef]
57. Martins, G.V.A.; Berlier, G.; Bisio, C.; Coluccia, S.; Pastore, H.O.; Marchese, L. Quantification of Brønsted acid sites in microporous catalysts by a combined FTIR and NH_3-TPD study. *J. Phys. Chem. C* **2008**, *112*, 7193–7200. [CrossRef]
58. Lee, K.Y.; Lee, S.W.; Ihm, S.K. Acid strength control in MFI zeolite for the methanol-to-hydrocarbons (MTH) reaction. *Ind. Eng. Chem. Res.* **2014**, *53*, 10072–10079. [CrossRef]
59. Galadima, A.; Muraza, O. From synthesis gas production to methanol synthesis and potential upgrade to gasoline range hydrocarbons: A review. *J. Nat. Gas. Sci. Eng.* **2015**, *25*, 303–316. [CrossRef]
60. Zhang, Q.; Wang, T.; Li, Y.; Xiao, R.; Vitidsant, T.; Reubroycharoen, P.; Wang, C.; Zhang, Q.; Ma, L. Olefin-rich gasoline-range hydrocarbons from oligomerization of bio-syngas over Ni/ASA catalyst. *Fuel Process. Technol.* **2017**, *167*, 702–710. [CrossRef]
61. Khadzhiev, S.N.; Magomedova, M.V.; Peresypkina, E.G. Mechanism of olefin synthesis from methanol and dimethyl ether over zeolite catalysts: A review. *Petrol. Chem.* **2014**, *54*, 245–269. [CrossRef]
62. Chang, C.D.; Lang, W.H.; Silvestri, A.J. Synthesis gas conversion to aromatic hydrocarbons. *J. Catal.* **1979**, *56*, 268–273. [CrossRef]
63. Wan, Z.; Wu, W.; Chen, W.; Yang, H.; Zhang, D. Direct synthesis of hierarchical ZSM-5 zeolite and its performance in catalyzing methanol to gasoline conversion. *Ind. Eng. Chem. Res.* **2014**, *53*, 19471–19478. [CrossRef]
64. Niu, X.; Gao, J.; Wang, K.; Miao, Q.; Dong, M.; Wang, G.; Fan, W.; Qin, Z.; Wang, J. Influence of crystal size on the catalytic performance of H-ZSM-5 and Zn/H-ZSM-5 in the conversion of methanol to aromatics. *Fuel Process. Technol.* **2017**, *157*, 99–107. [CrossRef]
65. Oseke, G.G.; Atta, A.Y.; Mukhtar, B.; Jibril, B.Y.; Aderemi, B.O. Highly selective and stable Zn-Fe/ZSM-5 catalyst for aromatization of propane. *Appl. Petrochem. Res.* **2020**, *10*, 55–65. [CrossRef]